Mon. Not. R. Astron. Soc. **000**, 1-14 (2014) Printed 19 June 2018 (MN LaTeX style file v2.2)

CO Tully-Fisher relation of star-forming galaxies at $z = 0.05 - 0.3$

Selçuk Topal,[1,2]⋆ Martin Bureau,[2] Alfred L. Tiley,[2,3] Timothy A. Davis,[4] and Kazufumi Torii[5]
[1] *Department of Physics, Van Yuzuncu Yil University, Van, 65080, Turkey*
[2] *Sub-department of Astrophysics, University of Oxford, Denys Wilkinson Building, Keble Road, Oxford OX1 3RH, U.K.*
[3] *Centre for Extragalactic Astronomy, Department of Physics, Durham University, South Road, Durham, DH1 3LE, U.K.*
[4] *School of Physics & Astronomy, Cardiff University, Queens Buildings, The Parade, Cardiff, CF24 3AA, UK,*
[5] *Nobeyama Radio Observatory, 462-2 Nobeyama Minamimaki-mura, Minamisaku-gun, Nagano 384-1305, Japan*

Accepted . Received ; in original form

ABSTRACT
The Tully-Fisher relation (TFR) is an empirical relation between galaxy luminosity and rotation velocity. We present here the first TFR of galaxies beyond the local Universe that uses carbon monoxide (CO) as the kinematic tracer. Our final sample includes 25 isolated, non-interacting star-forming galaxies with double-horned or boxy CO integrated line profiles located at redshifts $z \leqslant 0.3$, drawn from a larger ensemble of 67 detected objects. The best reverse K_s-band, stellar mass and baryonic mass CO TFRs are respectively $M_{K_\mathrm{s}} = (-8.4 \pm 2.9)\left[\log\left(\frac{W_{50}/\mathrm{km\ s^{-1}}}{\sin i}\right) - 2.5\right] + (-23.5 \pm 0.5)$, $\log\left(M_\star/M_\odot\right) = (5.2 \pm 3.0)\left[\log\left(\frac{W_{50}/\mathrm{km\ s^{-1}}}{\sin i}\right) - 2.5\right] + (10.1 \pm 0.5)$ and $\log\left(M_\mathrm{b}/M_\odot\right) = (4.9 \pm 2.8)\left[\log\left(\frac{W_{50}/\mathrm{km\ s^{-1}}}{\sin i}\right) - 2.5\right] + (10.2 \pm 0.5)$, where M_{K_s} is the total absolute K_s-band magnitude of the objects, $M_\star$ and M_b their total stellar and baryonic masses, and W_{50} the width of their line profile at 50% of the maximum. Dividing the sample into different redshift bins and comparing to the TFRs of a sample of local ($z = 0$) star-forming galaxies from the literature, we find no significant evolution in the slopes and zero-points of the TFRs since $z \approx 0.3$, this in either luminosity or mass. In agreement with a growing number of CO TFR studies of nearby galaxies, we more generally find that CO is a suitable and attractive alternative to neutral hydrogen (H I). Our work thus provides an important benchmark for future higher redshift CO TFR studies.

Key words: galaxies: kinematics and dynamics - galaxies: evolution - galaxies: spiral - galaxies:starburst - galaxies: elliptical and lenticular, cD

1 INTRODUCTION

The Tully-Fisher relation (TFR; Tully & Fisher 1977) is a well-established empirical correlation between the total stellar luminosity of a galaxy (tracing its total stellar mass) and its rotation velocity (tracing its total mass). It has been widely studied in the local Universe at both optical and near-infrared wavelengths, exhibiting a relatively small intrinsic scatter. Although the existence of a correlation between the stellar luminosity and the width of the neutral hydrogen (H I) line (roughly twice the maximum rotation velocity) of late-type galaxies (spirals and irregulars) was suggested before (Balkowski et al. 1974), Tully & Fisher (1977) showed that the relation could also be used for distance measurements. It also holds across a wide range of galaxy environments (e.g. Mould et al. 1993; Willick & Strauss 1998; Tully & Pierce 2000). The TFR relation is therefore a useful tool to indirectly probe the connection between the total mass-to-light ratio M/L and the total galaxy mass, and when studied as a function of redshift to test theories of galaxy formation (e.g. Steinmetz & Navarro 1999).

When a suitable kinematic tracer is available, it has been shown that the TFR also holds for early-type galaxies (ETGs, lenticulars and ellipticals; e.g. Neistein et al. 1999a; Magorrian & Ballantyne 2001; Gerhard et al. 2001; De Rijcke et al. 2007; Williams et al. 2010; Davis et al. 2011; den Heijer et al. 2015). Crucially, if lenticulars are "dead" spirals (i.e. spirals for which star formation has ceased), then their masses should remain roughly constant over time while their luminosity decreases. This would lead to an increase of their M/L and thus a shift of the TFR zero-point compared to that of spirals. Although some past works were unable to find such an offset (e.g. Dressler & Sandage 1983; Neistein et al. 1999b; Hinz et al. 2001, 2003), the results of other studies over the last decade or so do indicate one (e.g. Mathieu et al. 2002; Bedregal et al. 2006; Williams et al. 2010; Davis et al. 2011; den Heijer et al. 2015). In particular, Bedregal et al. (2006) found that the TFR of

⋆ E-mail: selcuktopal@yyu.edu.tr

lenticular galaxies lies about 1.2 mag below the spiral TFR with a scatter of 1.0 mag in the K_s-band, the largest offset found to date.

The H I emission line has been used heavily as the kinematic tracer for TFR studies (e.g. Tully & Fisher 1977; Tully & Pierce 2000; Pizagno et al. 2007). However, carbon-monoxide (CO) has also been shown to be an excellent kinematic tracer for TFR studies, as long as the CO emission extends beyond the peak of the galaxy rotation curve (Dickey & Kazes 1992; Schoniger & Sofue 1994a; Tutui & Sofue 1997; Lavezzi & Dickey 1998; Tutui et al. 2001; Ho 2007; Davis et al. 2011; Tiley et al. 2016a).

It is worth reflecting on the advantages of using CO line widths for TFR studies, compared with the widely used H I and optical emission lines. First and foremost, we can detect CO to much greater distances than H I; CO is routinely detected in normal star-forming galaxies at intermediate redshifts ($z \approx$ 1-3; e.g. Tacconi et al. 2010; Genzel et al. 2015) and in starbursting galaxies up to $z \approx 7$ (e.g. Riechers et al. 2009; Wang et al. 2011). Second, the beam size of CO observations is typically much smaller than that for H I, both for single-dish and interferometric observations, easily allowing to spatially resolve galaxies (and individual members within clusters of galaxies) even at high redshifts. Third, CO is less extended radially and more tightly correlated with the stellar component, and thus less affected by interactions between galaxies (Lavezzi & Dickey 1998). Finally, Hα probes warmer gas than CO and is primarily emitted from star-forming regions. CO is therefore a convenient and robust tracer to probe the TFR as a function of redshift, encompassing many galaxy morphologies and providing an independent test of other established measures.

CO line profiles show a wide variety of shapes for several reasons: inner velocity field and/or CO distribution differences, beam response along the disc, pointing errors (for single-dish observations), opacity effects, etc (Lavezzi & Dickey 1997). Nevertheless, even in ETGs (where the radial extent of the molecular gas can be very limited; Davis et al. 2013), Davis et al. (2011) have shown that galaxies with a double-horned or boxy integrated CO profile do yield accurate measurements of the maximum circular velocity (see also Tiley et al. 2016a), whereas galaxies with a single-peaked profile often do not.

We note that although $z > 0$ TFR studies based on optical observations exist (e.g. Conselice et al. 2005; Flores et al. 2006; Kassin et al. 2007; Puech et al. 2008), to our knowledge there is as yet no CO TFR work beyond the local Universe. Although studying the TFR of high-z disc galaxies comes at a price, e.g. the increased difficulty to determine exact galaxy morphologies and axial ratios (and therefore inclinations), much can be learnt about their formation and evolution if successful. For example, does the M/L ratios of distant galaxies differ from those of their local counterparts? If so, how are the stellar populations evolving, and what is the relative growth rate of luminous and dark matter? Our goals in this paper are thus twofold. First, to probe whether there is any evolution of the CO TFR as a function of redshift up to $z = 0.3$, by comparing the TFR of galaxies within our sample and from the literature (Tully & Pierce 2000; Tiley et al. 2016a). Second, to provide a local benchmark for future higher redshift CO TFR studies. Our work is the first attempt to construct a TFR for galaxies beyond the local Universe using CO emission as the kinematic tracer.

This paper is structured as follows. Section 2 describes the data used, while Section 3 discusses the sample selection. Section 4 presents the velocity measurements and TFR fits. The results are discussed in Section 5 and we conclude briefly in Section 6.

2 DATA AND PARENT SAMPLE

2.1 EGNoG CO sample

The Evolution of molecular Gas in Normal Galaxies (EGNoG) survey is a CO(1-0) survey of 31 galaxies at $z \approx 0.05$–0.5 by Bauermeister et al. (2013). All galaxies were selected from the Sloan Digitized Sky Survey Data Release 7 (SDSS DR7; York et al. 2000; Strauss et al. 2002; Abazajian et al. 2009) and the Cosmic Evolution Survey (COSMOS; Scoville et al. 2007) to be as representative as possible of the main sequence of star-forming galaxies (a correlation between star formation rate, SFR, and stellar mass, $M_\star$) at the redshifts concerned.

First, only galaxies with a spectroscopic redshift (essential for follow-up CO observations) as well as $4 \leqslant M_\star \leqslant 30 \times 10^{10}\ M_\odot$ and $4 \leqslant$ SFR $\leqslant 100\ M_\odot\ \mathrm{yr}^{-1}$ (to restrict the sample to main sequence objects) were selected. Galaxies harbouring an active galactic nucleus (AGN) were then rejected, as diagnosed from standard emission line ratios measured in the SDSS spectra (see Kauffmann et al. 2003 and Section 3.1.2). Interacting galaxies were also excluded via a visual inspection of the SDSS images, although we revisit this issue in Section 3.

The galaxies to be observed in CO were selected randomly from all the galaxies meeting the above selection criteria. CO(1-0) observations of all 31 EGNoG galaxies were obtained using the Combined Array for Research in Millimeter-wave Astronomy (CARMA) and were spatially integrated to generate total spectra. The core of our sample is composed of the 24 EGNoG galaxies that were reliably detected according to Bauermeister et al. (2013), all at $z \approx 0.05$–0.3 and all from SDSS (i.e. none of the COSMOS galaxies at $z \approx 0.5$ was reliably detected in CO). A few of these galaxies are luminous infrared galaxies (LIRGs, with infrared luminosities $10^{11} < L_{\rm IR} < 10^{12}\ L_\odot$), but none is an ultra-luminous infrared galaxy (ULIRG, with $L_{\rm IR} > 10^{12}\ L_\odot$). See Bauermeister et al. (2013) for more details of the sample selection, observations and data reduction.

2.2 Additional CO data

Additional CO data for galaxies within the EGNoG redshift range were taken from the literature. Mirabel et al. (1990) detected CO in 19 LIRGs and 9 ULIRGs at $z = 0.01$–0.1, complementing the work of Sanders et al. (1991) who published CO line profiles for an additional 52 LIRG and 8 ULIRG detections at $z = 0.01$–0.1. Tutui et al. (2000) detected 10 LIRGs and 3 ULIRGS at $z = 0.05$–0.2. In addition, Matsui et al. (2012) detected CO in 7 galaxies at $z = 0.08$–0.2 and Cortese et al. (2017) published the CO line profiles of 5 galaxies at $z \approx 0.2$. See the related papers for more details of the observations and data reduction. Overall, we thus obtained the CO profiles of an additional 113 galaxies from the literature, 43 of which are in the redshift range $z = 0.05$–0.3 we aim to study, while the rest are located much closer at $z < 0.05$.

Combining the EGNoG CO detections (24 galaxies) with the additional literature detections (43 galaxies), we obtain a parent sample of 67 galaxies with integrated CO profiles at $z = 0.05$–0.3.

Homogenous samples of galaxies are necessary for TFR studies. To build such samples, environmental effects (e.g. interactions and mergers) and intrinsic properties (e.g. inclination and luminosities) have to be considered first. See Section 3 for detailed explanations of the selection criteria applied to our parent sample, to construct the more homogenous samples of galaxies necessary for TFR studies.

2.3 Near-infrared photometry

Stellar luminosities are also required to construct TFRs. Near-infrared photometry is superior to that at shorter wavelengths as it is less affected by dust extinction. This is particularly crucial for highly inclined galaxies and dusty high-redshift objects. For example, if left uncorrected dust extinction can cause an error $\gtrsim 1$ mag at optical wavelengths (e.g. B-band or ≈ 440 nm), while the uncertainties at K-band (≈ 2.2 µm) are much less (≈ 0.1 mag; Noordermeer & Verheijen 2007). Longer wavelengths (e.g. mid-infrared) are affected by dust emission and are thus also inappropriate. Partially as a results of these effects, but also because the M/L of stellar populations varies the least at K-band (e.g. Maraston 2005), the scatter of the TFR is correspondingly minimised in this band (Verheijen 2001). The K-band is therefore the optimal choice of passband to measure the galaxy luminosities.

The total apparent K_s-band magnitudes of all our sample galaxies were obtained from the Two Micron All Sky Survey (2MASS; Jarrett et al. 2000; Skrutskie et al. 2006) and are listed in Table 1. For most galaxies, we adopted the *k_m_ext* parameter from the 2MASS Extended Source Catalog (XSC; Jarrett et al. 2000), i.e. the integrated K_s-band magnitude from an extrapolated fit. For galaxies that are not extended in 2MASS and thus not in the XSC, we adopted the *k_m* parameter, i.e. the default integrated K_s-band magnitude from the 2MASS Point Source Catalog (PSC; Skrutskie et al. 2006), measured in a $4\farcs0$ radius aperture. The width of the 2MASS optical system point spread function (PSF) meant that 2–15% of the total fluxes fell outside this aperture, but after applying curve-of-growth corrections the standard aperture measurements accurately reflect the fluxes within "infinite" apertures capturing all of the sources' emission (Skrutskie et al. 2006).

For the four galaxies in our sample that do not have 2MASS data available, we adopted the *kAperMag6* parameter, i.e. the K_s-band $5\farcs7$ aperture integrated magnitude from the United Kingdom Infrared Telescope (UKIRT) Infrared Deep Sky Survey (UKIDSS; Lawrence et al. 2007; Casali et al. 2007). All magnitudes quoted in this paper are Vega magnitudes (see Table 1).

2.4 Inclinations

The inclination of each galaxy is necessary to deproject its measured velocity width. This was calculated using each galaxy's axial ratio from its SDSS r-band image (specifically the *expAB_r* and *expABErr_r* parameters from the SDSS Data Release 12 catalogue; Alam et al. 2015) and the standard expression (Holmberg 1958)

$$i_{b/a} = \cos^{-1}\left(\sqrt{\frac{q^2 - q_0^2}{1 - q_0^2}}\right) , \tag{1}$$

where q is the ratio of the semi-minor (b) to the semi-major (a) axis of the galaxy, q_0 is the intrinsic axial ratio when the galaxy is seen edge-on ($q_0 \equiv c/a$), and $q_0 = 0.2$ is assumed here (appropriate for late-type systems; Tully & Fisher 1977; Pierce & Tully 1988).

2.5 Stellar masses

The most common technique for measuring stellar masses is to fit observed spectral energy distributions (SEDs) to templates generated from stellar population synthesis models. However, each method has its own degeneracies. Mobasher et al. (2015) tested the consistency of stellar masses measured using different methods (including Bruzual & Charlot 2003, from which the stellar masses in this study are derived) and found good agreement between the input and estimated stellar masses when using the median of the stellar masses of individual galaxies derived from different methods.

In our study, the stellar mass of each galaxy was taken from the Max Planck Institute for Astrophysics-Johns Hopkins University Data Release 8[1] (MPA-JHU DR8). Each mass was derived by fitting the galaxy SDSS $ugriz$ photometry to a grid of models from the Bruzual & Charlot (2003) stellar population synthesis code, encompassing a wide range of star formation histories. The mass and its uncertainty are defined as the median of the probability distribution and half the difference between the 16th and 84th percentiles of the distribution (1σ error), respectively.

For the five galaxies that do not have their stellar mass calculated by MPA-JHU (indicated by BPT class 0 in Table 1), we obtained stellar masses from *kcorrect* (see Section 2.7), that also uses Bruzual & Charlot's (2003) stellar population synthesis code. Population synthesis codes can change stellar masses by around 0.2 dex (e.g. Mobasher et al. 2015; Roediger & Courteau 2015). We therefore assumed the same 0.2 dex uncertainty for those five galaxies. The stellar masses of all the galaxies in our sample (both EGNoG and others) are listed in Table 1.

As our galaxies are located across the redshift range $z =$ 0.05–0.3, redshift effects and photometric uncertainties (that both tend to increase with redshift) must also be considered. Only 4 galaxies in our sample are located at $z \approx 0.3$, while the rest are located at $z \leqslant 0.2$. Mobasher et al. (2015) found no redshift-dependent bias at $z = 0$–4 for stellar masses measured with the same input parameters but using different methods/codes. However, the signal-to-noise ratio (S/N) of photometric data can also introduce further scatter in the stellar masses. Although this effect becomes dominant for faint galaxies with low photometric S/N ratios, Mobasher et al. (2015) found that when the input parameters are left free, there is an offset in the stellar masses at high S/N ratios for most of the methods. This indicates that the errors in the stellar masses are not necessarily caused by photometric uncertainties (Mobasher et al. 2015).

2.6 Baryonic masses

The baryonic mass of a galaxy consists of all visible components, i.e. both gas and stars. The molecular gas masses, M_{H_2}, of all galaxies in our sample were taken from the related papers (Mirabel et al. 1990; Sanders et al. 1991; Tutui et al. 2000; Matsui et al. 2012; Bauermeister et al. 2013; Cortese et al. 2017), whereas the stellar masses were derived as described in the previous sub-section. Finally, to estimate the atomic gas masses, M_{HI}, we used the molecular-to-atomic gas mass relation of Saintonge et al. (2011, i.e. M_{H_2} / M_{HI}, see their Table 4). The baryonic masses, M_{b}, of all galaxies are listed in Table 1.

2.7 Absolute magnitudes and K corrections

Because our galaxies span the redshift range $z = 0.01$–0.3, the portion of their spectra intercepted by the K_s filter varies from object to object, and we must correct the apparent magnitudes measured to rest-frame ($z = 0$) measurements. This so-called K-correction is fully described in Hogg et al. (2002), and it was applied to our

[1] https://www.sdss3.org/dr10/spectro/galaxy_mpajhu.php

Table 1. General galaxy parameters for the initial and final sub-samples.

Galaxy (1)	SDSS name (2)	z (3)	m_{K_s} (mag) (4)	$\log(M_\star/M_\odot)$ (5)	$\log(M_b/M_\odot)$ (6)	BPT class (7)	Notes (8)
			Final sub-sample galaxies				
G1	SDSSJ091957.00+013851.6	0.176	14.84 ± 0.15	10.9 ± 0.1	11.1 ± 0.1	1	PSC, Cortese et al. (2017)
G2	SDSSJ140522.72+052814.6	0.195	14.84 ± 0.02	11.0 ± 0.1	11.1 ± 0.1	2	UKIRT, Cortese et al. (2017)
G3	SDSSJ111628.07+291936.1	0.046	11.83 ± 0.08	11.0 ± 0.1	11.0 ± 0.1	1	Tutui et al. (2000)
G4	SDSSJ231332.46+133845.3	0.081	13.29 ± 0.15	11.0 ± 0.1	11.1 ± 0.1	1	
G5	SDSSJ141906.70+474514.8	0.072	12.43 ± 0.09	10.9 ± 0.1	10.9 ± 0.1	1	Tutui et al. (2000)
G6	SDSSJ233455.23+141731.0	0.062	12.11 ± 0.06	11.0 ± 0.1	11.1 ± 0.1	1	
G7	SDSSJ221938.11+134213.9	0.084	12.59 ± 0.12	11.2 ± 0.1	11.3 ± 0.1	1	
G8	SDSSJ223528.63+135812.6	0.183	13.51 ± 0.18	11.4 ± 0.1	11.5 ± 0.1	2	
G9	SDSSJ100518.63+052544.2	0.166	14.65 ± 0.11	10.8 ± 0.1	10.8 ± 0.1	2	PSC
G10	SDSSJ105527.18+064015.0	0.173	14.52 ± 0.10	11.0 ± 0.1	11.1 ± 0.1	2	PSC
G11	SDSSJ124252.54+130944.2	0.175	14.84 ± 0.13	10.8 ± 0.2	10.9 ± 0.2	1	PSC
G12	SDSSJ091426.24+102409.6	0.176	13.19 ± 0.19	11.5 ± 0.1	11.5 ± 0.1	2	
G13	SDSSJ114649.18+243647.7	0.177	14.74 ± 0.09	11.1 ± 0.1	11.1 ± 0.1	2	PSC
G14	SDSSJ092831.94+252313.9	0.283	15.06 ± 0.14	11.2 ± 0.2	11.3 ± 0.1	1	PSC
G15	SDSSJ133849.18+403331.7	0.285	14.04 ± 0.19	11.3 ± 0.2	11.4 ± 0.1	1	
G16	SDSSJ142735.69+033434.2	0.246	14.58 ± 0.02	11.3 ± 0.1	11.3 ± 0.1	2	UKIRT, Cortese et al. (2017)
G17	SDSSJ144518.88+025012.3	0.190	14.86 ± 0.15	11.2 ± 0.1	11.2 ± 0.1	1	PSC, Cortese et al. (2017)
G18	SDSSJ151337.28+041921.1	0.175	15.43 ± 0.03	10.8 ± 0.1	10.8 ± 0.1	2	UKIRT, Cortese et al. (2017)
G19	SDSSJ095904.41+024957.8	0.119	15.35 ± 0.20	10.4 ± 0.1	10.7 ± 0.1	1	PSC, Matsui et al. (2012)
G20	SDSSJ100107.15+022519.5	0.121	15.20 ± 0.19	10.0 ± 0.2	10.2 ± 0.2	0	PSC, Matsui et al. (2012)
G21	2MASXJ17320995+2007424	0.050	12.20 ± 0.07	10.4 ± 0.2	10.6 ± 0.1	0	Tutui et al. (2000)
G22	SDSSJ145114.64+164143.6	0.050	11.74 ± 0.06	10.7 ± 0.1	10.8 ± 0.0	3	Tutui et al. (2000)
G23	2MASXJ16381190-6826080	0.050	10.93 ± 0.04	10.6 ± 0.2	11.0 ± 0.1	0	Mirabel et al. (1990)
G24	2MASXJ10200023+0813342	0.050	13.08 ± 0.16	10.6 ± 0.1	10.9 ± 0.0	5	Sanders et al. (1991)
G25	SDSSJ135751.77+140527.3	0.099	12.91 ± 0.11	10.8 ± 0.1	10.8 ± 0.1	1	
			Remaining initial sub-sample galaxies				
G26	2MASX J01385289-1027113	0.050	12.78 ± 0.12	9.9 ± 0.2	10.4 ± 0.1	0	Mirabel et al. (1990)
G27	SDSSJ100318.58+025504.8	0.105	15.51 ± 0.21	10.1 ± 0.1	10.2 ± 0.1	1	PSC, Matsui et al. (2012)
G28	SDSSJ095933.75+014905.8	0.133	14.69 ± 0.11	10.5 ± 0.1	10.7 ± 0.1	1	PSC, Matsui et al. (2012)
G29	SDSSJ100051.21+014027.1	0.166	15.04 ± 0.14	10.5 ± 0.1	10.6 ± 0.1	1	PSC, Matsui et al. (2012)
G30	SDSSJ100045.29+013847.4	0.220	14.63 ± 0.02	11.2 ± 0.1	11.2 ± 0.1	3	UKIRT, Matsui et al. (2012)
G31	SDSSJ234311.26+000524.3	0.097	13.52 ± 0.17	10.7 ± 0.1	10.8 ± 0.1	1	
G32	SDSSJ211527.81-081234.4	0.091	12.94 ± 0.12	10.6 ± 0.1	10.6 ± 0.1	1	
G33	2MASXJ02211866+0656431	0.098	12.63 ± 0.11	10.4 ± 0.2	10.9 ± 0.1	0	Tutui et al. (2000)
G34	SDSSJ105733.59+195154.2	0.077	13.10 ± 0.12	10.7 ± 0.1	10.8 ± 0.1	1	
G35	SDSSJ141601.21+183434.1	0.055	12.27 ± 0.09	11.1 ± 0.1	11.1 ± 0.1	2	
G36	SDSSJ100559.89+110919.6	0.076	12.92 ± 0.13	11.0 ± 0.1	11.0 ± 0.1	1	
G37	SDSSJ002353.97+155947.8	0.192	13.12 ± 0.16	11.3 ± 0.1	11.4 ± 0.1	1	
G38	SDSSJ134322.28+181114.1	0.178	14.11 ± 0.14	11.3 ± 0.1	11.4 ± 0.1	2	
G39	SDSSJ130529.30+222019.8	0.190	14.42 ± 0.08	11.0 ± 0.1	11.0 ± 0.1	1	PSC
G40	SDSSJ090636.69+162807.1	0.301	15.30 ± 0.15	11.2 ± 0.2	11.3 ± 0.2	1	PSC

Notes: Column 3: redshift, taken from Bauermeister et al. (2013) for EGNoG galaxies and from the original paper otherwise (see Sections 2.1 and 2.2). Column 4: total Vega apparent magnitude, taken from the 2MASS PSC survey (Jarrett et al. 2000) of UKIRT (Lawrence et al. 2007; Casali et al. 2007) for the galaxies so noted in Column 8 and from the 2MASS XSC survey (Skrutskie et al. 2006) otherwise (see Section 2.3). Column 5: stellar mass, taken from MPA-JHU DR8 (see Section 2.5). Column 6: baryonic mass, as determined in Section 2.6. Column 7: BPT class, following the original Baldwin et al. (1981) classification (see Section 3.1.2). Column 8: source of the data for sample galaxies not belonging to EGNoG, as well as galaxies not found in the 2MASS XSC survey (PSC and UKIRT).

data using the publicly available code *kcorrect*[2] version 4 (Blanton & Roweis 2007). Using the spectroscopic redshifts provided (see Table 1), *kcorrect* finds the intrinsic spectrum that best represents the observed galaxy SED (here SDSS $ugriz$ and 2MASS or UKIRT JHK total apparent magnitudes) by fitting templates from the Bruzual & Charlot (2003) stellar population synthesis code. The templates have been optimised to minimise the residuals between the observed and modelled galaxy fluxes.

The *kcorrect* routine determines absolute magnitudes for each galaxy by calculating the distance modulus, accounting for the angular diameter distance and cosmological surface brightness dimming. We adopt here the cosmological parameters from the Planck results (Planck Collaboration et al. 2016). A Galactic extinction correction is also applied using the extinction maps of Schlegel et al. (1998). The 2MASS Vega magnitudes were transformed to AB magnitudes to use *kcorrect*, but were then transformed back to Vega magnitudes for use in this paper following the application of K-correction. Fully corrected total absolute K_s-band Vega magnitudes for all our sample galaxies are listed in Table 2.

[2] http://kcorrect.org/

Table 2. TFR galaxy parameters for the initial and final sub-samples.

Galaxy	M_{K_s} (mag)	W_{50} (km s^{-1})	b/a	$i_{b/a}$ (°)	$W_{50}/\sin i$ (km s^{-1})	Notes
(1)	(2)	(3)	(4)	(5)	(6)	(7)
Final sub-sample galaxies						
G1	-24.87 ± 0.03	189.7 ± 4.0	0.66 ± 0.01	49.68 ± 0.02	248.7 ± 6.6	
G2	-24.66 ± 0.04	512.3 ± 12.9	0.46 ± 0.01	64.70 ± 0.01	566.7 ± 14.7	
G3	-24.72 ± 0.08	176.1 ± 20.1	0.68 ± 0.01	48.71 ± 0.01	234.4 ± 26.8	
G4	-24.49 ± 0.15	217.3 ± 43.1	0.63 ± 0.01	52.72 ± 0.01	273.1 ± 54.3	
G5	-25.06 ± 0.09	230.2 ± 10.6	0.63 ± 0.01	52.10 ± 0.01	291.5 ± 13.6	
G6	-25.11 ± 0.07	417.4 ± 61.7	0.59 ± 0.01	55.27 ± 0.01	507.8 ± 75.1	
G7	-25.24 ± 0.12	483.2 ± 36.5	0.62 ± 0.01	53.57 ± 0.01	600.5 ± 45.5	
G8	-26.06 ± 0.18	586.4 ± 18.5	0.44 ± 0.01	66.40 ± 0.02	639.9 ± 20.7	
G9	-24.59 ± 0.11	298.7 ± 33.0	0.84 ± 0.02	33.34 ± 0.04	543.4 ± 67.2	
G10	-24.82 ± 0.10	417.2 ± 25.4	0.72 ± 0.02	44.88 ± 0.03	591.3 ± 39.6	
G11	-24.51 ± 0.13	253.9 ± 24.4	0.45 ± 0.02	65.85 ± 0.02	278.2 ± 26.9	
G12	-26.23 ± 0.19	464.0 ± 21.3	0.85 ± 0.02	33.08 ± 0.03	850.2 ± 53.6	
G13	-24.62 ± 0.09	373.5 ± 50.9	0.52 ± 0.01	60.98 ± 0.02	427.2 ± 58.4	
G14	-25.47 ± 0.14	535.0 ± 35.1	0.54 ± 0.02	59.26 ± 0.02	622.5 ± 41.9	
G15	-26.47 ± 0.19	265.1 ± 16.9	0.87 ± 0.02	30.27 ± 0.04	525.8 ± 47.0	
G16	-25.49 ± 0.04	408.3 ± 14.1	0.62 ± 0.02	53.12 ± 0.02	510.4 ± 20.0	
G17	-24.66 ± 0.15	421.7 ± 2.9	0.76 ± 0.02	41.03 ± 0.03	642.4 ± 22.5	
G18	-23.85 ± 0.05	425.2 ± 12.9	0.46 ± 0.02	65.05 ± 0.02	467.0 ± 15.0	
G19	-23.19 ± 0.21	372.2 ± 28.2	0.69 ± 0.02	48.03 ± 0.02	500.6 ± 39.6	
G20	-23.44 ± 0.19	336.1 ± 25.5	0.51 ± 0.02	61.39 ± 0.03	382.9 ± 29.5	
G21	-24.55 ± 0.08	424.1 ± 6.9	0.50 ± 0.05	62.11 ± 0.06	479.8 ± 17.8	
G22	-24.80 ± 0.07	256.3 ± 16.1	0.81 ± 0.01	36.90 ± 0.01	426.8 ± 27.1	
G23	-25.70 ± 0.05	572.4 ± 16.0	0.50 ± 0.05	62.11 ± 0.06	647.6 ± 28.2	
G24	-23.60 ± 0.16	163.0 ± 11.8	0.22 ± 0.01	84.42 ± 0.01	163.0 ± 11.8	
G25	-25.25 ± 0.11	684.4 ± 87.5	0.73 ± 0.01	43.85 ± 0.01	987.8 ± 126.6	
Remaining initial sub-sample galaxies						
G26	-23.86 ± 0.12	130.5 ± 29.7	0.59 ± 0.01	55.79 ± 0.01	157.8 ± 35.9	s
G27	-22.74 ± 0.21	299.9 ± 55.1	0.76 ± 0.02	41.45 ± 0.03	453.0 ± 84.7	s
G28	-24.07 ± 0.11	329.1 ± 38.7	0.76 ± 0.02	41.74 ± 0.02	494.3 ± 59.7	s
G29	-24.21 ± 0.15	140.8 ± 26.5	0.81 ± 0.02	36.30 ± 0.04	237.8 ± 46.2	s
G30	-25.18 ± 0.04	524.1 ± 254.5	0.52 ± 0.02	60.58 ± 0.02	601.6 ± 292.2	s
G31	-24.64 ± 0.17	135.8 ± 42.4	0.63 ± 0.01	52.67 ± 0.01	170.9 ± 53.4	s
G32	-25.07 ± 0.12	164.8 ± 72.7	0.50 ± 0.01	62.16 ± 0.01	186.4 ± 82.2	s
G33	-25.41 ± 0.11	239.7 ± 8.7	0.84 ± 0.08	33.63 ± 0.15	432.9 ± 100.1	s
G34	-24.54 ± 0.12	402.9 ± 93.3	0.70 ± 0.01	46.57 ± 0.01	554.8 ± 128.5	s
G35	-24.68 ± 0.09	164.8 ± 24.4	0.27 ± 0.01	79.34 ± 0.01	167.7 ± 24.8	s
G36	-24.73 ± 0.14	248.0 ± 40.3	0.57 ± 0.01	56.88 ± 0.01	296.2 ± 48.2	s
G37	-26.54 ± 0.16	398.0 ± 37.5	0.54 ± 0.02	59.21 ± 0.02	463.3 ± 44.0	s
G38	-25.32 ± 0.14	354.8 ± 52.8	0.67 ± 0.02	49.08 ± 0.02	469.6 ± 70.6	s
G39	-25.14 ± 0.08	194.0 ± 25.6	0.76 ± 0.02	41.40 ± 0.03	293.4 ± 39.7	s
G40	-25.22 ± 0.15	139.4 ± 12.1	0.77 ± 0.02	40.53 ± 0.04	214.6 ± 20.6	s

Notes: Column 1 lists the galaxies as in Table 1. Column 2: corrected total Vega absolute magnitudes, calculated as described in Section 2.7. Column 3: velocity widths, calculated as described in Section 4.1. Column 4: axial ratios, taken from the SDSS r-band images (see Section 2.4). Column 5: inclinations, calculated as described in Section 2.4. Column 7: reasons why galaxies were excluded from the final sample ("s" stands for a single Gaussian integrated line profile).

3 SAMPLE SELECTION

To draw a more homogenous initial sub-sample of galaxies from the parent sample, we applied the further selection criteria described below. We then drew a final sub-sample for which all galaxies have a double-horned or boxy CO integrated line profile, i.e. galaxies where the gas likely reaches the flat part of the rotation curve (e.g. Lavezzi & Dickey 1997; Davis et al. 2011).

3.1 Initial sub-sample

3.1.1 Galaxy interactions

The TFR is only meaningful if the kinematic tracer used is rotationally-supported and in equilibrium. It is thus important to remove from our sample galaxies that are strongly interacting. For the additional literature data, all galaxies showing sings of interactions in SDSS images were excluded, as done by construction for the EGNoG sample. We also excluded all galaxies described as interacting in the original papers or in the NASA/IPAC Extragalactic Database[3] (NED), as well as objects showing signs of interactions in archival *Hubble Space Telescope* (*HST*) images (minor disturbances, bridges, tails and mergers). These checks resulted in the rejection of 22 objects from the parent sample (none from EGNoG), leaving all 24 EGNoG galaxies and 21 additional objects from the literature.

[3] https://ned.ipac.caltech.edu

3.1.2 AGN

As the emission from active galactic nuclei (AGN) can contaminate the measured stellar luminosities, we also removed galaxies with a strong AGN from our TFR sample. We did this using the MPA-JHU classifications of the galaxies' optical emission line ratios from the SDSS spectra (Brinchmann et al. 2004), inspired by the Baldwin et al. (1981) diagnostic diagrams (BPT diagrams). According to this, galaxies are divided into "Unclassifiable" (BPT class -1), "Not Used" (BPT class 0), "Star Forming" (BPT class 1), "Low S/N Star Forming" (BPT class 2), "Composite" (BPT class 3), "AGN" (BPT class 4) and "Low S/N AGN" (BPT class 5) categories.

None of the EGNoG galaxies (by construction) or remaining additional galaxies from the literature harbours a strong AGN (BPT class 4), thus leaving 45 mostly star-forming or low S/N star-forming galaxies (i.e. BPT class 1 or 2 objects) for our TFR analyses, including all 24 ENGoG galaxies and 21 additional objects from the literature. (see Table 1).

3.1.3 Inclination

As a galaxy approaches a face-on orientation ($i = 0°$), the uncertainty in the inclination increases. This is particularly problematic as the inclination correction to the velocity width measured is then also large ($\sin^{-1} i$). We therefore only retain galaxies with $i \geqslant 30°$ (a standard cutoff; see e.g. Pierce & Tully 1988; Tiley et al. 2016a), leading us to exclude 5 of the 45 remaining galaxies (3 from EGNoG and 2 from the literature). This results in an initial sub-sample of 40 galaxies, 21 from EGNoG and 19 from the literature. They are listed in Table 1.

This stark reduction in the size of the literature sample (from 43 to 19 galaxies) is unfortunate but perhaps unsurprising, as LIRGs and ULIRGs are often disturbed and the fraction of active galaxies increases with increasing infrared luminosity (Veilleux et al. 1999, 2002; Wang et al. 2006). Nevertheless, we increase the EGNoG sample by about 90% by including the remaining literature galaxies.

3.1.4 ULIRGs

Although the parent sample has many ULIRGs, there is no remaining ULIRG in the initial sub-sample, as a result of excluding all galaxies showing signs of mergers/interactions. This supports the idea that ULIRGs at $z \lesssim 0.3$ are dominated by mergers/interactions (Armus et al. 1987; Melnick & Mirabel 1990; Surace et al. 2000; Bushouse et al. 2002).

We also checked the SFRs of our initial sub-sample galaxies, to verify whether any ULIRG remained. The SFRs of our initial sub-sample galaxies were again obtained from the work of the MPA-JHU group[4]. The SFR range of LIRGs and ULIRGs is 10–170 and 170–1700 $M_\odot$ yr^{-1}, respectively (e.g. Kennicutt 1998; Alonso-Herrero 2013; Carpineti et al. 2015). None of the 40 galaxies in our initial sub-sample has a SFR greater than 75 $M_\odot$ yr^{-1}, 15 have $10 < \text{SFR} < 75$ $M_\odot$ yr^{-1}, and the rest (25) have SFR$<$ 10 $M_\odot$ yr^{-1}. The average SFR of our initial sub-sample and the final sub-sample (see the sub-section below) is 18 and 15 $M_\odot$ yr^{-1}, respectively, again strengthening the suggestion that our sub-samples do not include any ULIRG.

We also note that about 60% of the galaxies in the initial sub-sample have a SFR smaller than the typical SFR of LIRGs. This indicates that the resulting CO TFRs are not dominated by LIRGs.

In summary, none of the galaxies in our initialsub-sample show any sign of interactions, and they mostly are purely star-forming galaxies with an inclination angle $i \geqslant 30°$.

3.2 Final sub-sample

A kinematic tracer that extends significantly past the turnover of the galaxy circular velocity curve into its "flat" velocity regions will usually yield a double-horned or boxy integrated line profile (see e.g. Davis et al. 2011). Our line profile analysis in Section 4.1 indicates that 25 of the 40 galaxies in our initial sub-sample have a double-horned or boxy profile and are thus likely to yield reliable velocity width measurements. The remaining 15 galaxies have line profiles best represented by a single Gaussian.

There are several reasons for a galaxy's integrated CO profile to exhibit a single-Gaussian shape (see Section 1). The most obvious, however, is that the CO-emitting gas does not have sufficient radial extent to probe beyond the galaxy's circular velocity turnover. In these cases, such galaxies clearly warrant exclusion from our TFR analysis in order to avoid biasing our best fit relation to higher intercepts (lower velocities), or artificially increasing our measure of the TFR scatter. As clearly seen from Figure 1 panels (a), (c) and (e), those systems exhibiting single-Gaussian integrated CO line profiles tend to have lower rotational velocities ($W_{50}/\sin i < 10^{2.5}$ km s^{-1}) than those with double-horned or boxy profiles, lending significance to the postulate that the CO line profile width underestimates the total rotation velocity for these systems. We thus exclude them from our final sub-sample. The excluded systems are labeled as such in column 7 of Table 2.

Overall, our final sub-sample of inactive galaxies with inclination $i \geqslant 30°$ and a double-horned or boxy integrated line profile is thus composed of 25 galaxies (from an initial sub-sample of 40), 12 from EGNoG and 13 additional galaxies from the literature. For our analyses, we construct TFR relations and report the results for both the final and initial sub-samples. However, we base our discussion on the higher quality final sub-sample only.

4 VELOCITY MEASUREMENTS AND TULLY-FISHER RELATIONS

4.1 Velocity widths

The second observable required to construct a TFR is a measurement of the circular velocity, or in the case of integrated spectra (half) the width of the line profile. The line widths at 20% (W_{20}; e.g. Tully & Fisher 1977; Tully & Pierce 2000; Davis et al. 2011) and 50% (W_{50}; e.g. Schoniger & Sofue 1994b; Lavezzi & Dickey 1998; Tiley et al. 2016a) of the peak intensity are commonly used measures of the maximum rotational velocity, but Lavezzi & Dickey (1997) found that W_{50} has smaller uncertainties and suffers the least bias. We thus adopt W_{50} as our measure of (twice) the rotation velocity.

Tiley et al. (2016a) tested four fitting functions when using CO integrated spectra in the context of TFR studies. Using simulated spectra generated from modelled galaxies, they found that the Gaussian Double Peak function (a quadratic function bordered by a half-Gaussian on either side; see below) was the most appropriate, in the sense that it yielded the most consistent velocity width

[4] https://www.sdss3.org/dr10/spectro/galaxy_mpajhu.php

measures as a function of both amplitude-to-noise ratio (A/N) and inclination, this for a wide range of maximum circular velocities. The only exceptions were at very low inclinations and circular velocities, where the single-peaked Gaussian function was unsurprisingly better suited (as even intrinsically double-horned spectra appear single-peaked when spread over only few velocity channels).

Here, we thus fit all our integrated spectra with both the Gaussian Double Peak function and the single Gaussian function, and we adopt the fit with the lowest reduced χ^2 ($\chi^2_{\rm red}$, defined in the standard manner; but see below). The fits were carried out with the package MPFIT (Markwardt 2009), that employs a Levenberg-Marquardt minimisation algorithm. To avoid local minima, in each case we ran MPFIT several times with different initial guesses. The fitting parameters with the smallest $|1 - \chi^2_{\rm red}|$ value were taken as the best fit.

The form of the Gaussian Double Peak function is

$$f(v) = \begin{cases} A_{\rm G} \times {\rm e}^{\frac{-[v-(v_0-w)]^2}{2\sigma^2}} & v < v_0 - w \\ A_{\rm C} + a\,(v - v_0)^2 & v_0 - w \leqslant v \leqslant v_0 + w \\ A_{\rm G} \times {\rm e}^{\frac{-[v-(v_0+w)]^2}{2\sigma^2}} & v > v_0 + w \end{cases} , \quad (2)$$

where v is the velocity, $A_{\rm C} > 0$ is the flux at the central velocity v_0, $A_{\rm G} > 0$ is the peak flux of the half Gaussians on both sides (centred at velocities $v_0 \pm w$), $w > 0$ is the half-width of the central parabola, $\sigma > 0$ is the width of the profile edges, and $a \equiv (A_{\rm G} - A_{\rm C})/w^2$.

The velocity width W_{50} can then be easily calculated analytically. Defining

$$A_{\rm max} \equiv \begin{cases} A_{\rm C} & \text{if } A_{\rm C} \geqslant A_{\rm G} \\ A_{\rm G} & \text{if } A_{\rm C} < A_{\rm G} \end{cases} , \quad (3)$$

then if $A_{\rm G} \geqslant A_{\rm max}/2$ (i.e. the central parabola is either concave, as expected for a standard double-horned profile, or slightly convex), the profile width is determined by the two half-Gaussians and W_{50} is given by

$$W_{50} = 2\,(w + \sqrt{2\ln 2}\,\sigma) \ . \quad (4)$$

If $A_{\rm G} < A_{\rm max}/2$ (i.e. the central parabola is strongly convex), the profile width is determined by the central parabola but the profile is in fact not really double-horned and it is preferable to adopt a single Gaussian fit irrespective of the $\chi^2_{\rm red}$ value.

The single Gaussian function is given by

$$f(v) = A\,{\rm e}^{\frac{-(v-v_0)^2}{2\sigma^2}} \ , \quad (5)$$

where $A > 0$ is the flux of the peak at the central (and mean) velocity v_0, and $\sigma > 0$ is the width of the profile (root mean square velocity). The velocity width W_{50} is then given by

$$W_{50} = 2\sqrt{2\ln 2}\,\sigma \ , \quad (6)$$

as for the Gaussian Double Peak function with $w = 0$.

The uncertainty on the velocity width, ΔW_{50}, is estimated by generating 150 realisations of the best-fit model. Random Gaussian noise (with a root mean square equal to that in line-free channels of the spectrum) is added to each realisation, which is then fit as described above. Finally, ΔW_{50} is taken as the standard deviation of the measured velocity width distribution.

We further note here that while $A_{\rm max}/2$ is the mathematically convenient threshold to determine whether one should use the Gaussian Double Peak function or the single Gaussian function, Tiley et al. (2016a) established that $2A_{\rm max}/3$ is a more practical threshold to use. We therefore adopt this convention, and use the Gaussian Double Peak function (Eqs. 2 and 4) when $A_{\rm G} \geqslant 2A_{\rm max}/3$ and the single Gaussian function (Eqs. 5 and 6) otherwise.

4.2 Tully-Fisher relations

We constructed $M_{K_{\rm s}}$ TFRs for the galaxies in both our initial and final sub-samples. We used a standard form for the TFR,

$$M_{K_{\rm s}} = a \left[\log \left(\frac{W_{50}/\sin i}{\rm km\ s^{-1}} \right) - 2.5 \right] + b \ , \quad (7)$$

where a is the slope and b the zero-point of the relation. We fit this linear relationship to the data using the MPFITEXY routine (Williams et al. 2010), that uses the MPFIT package. The intrinsic scatter ($\sigma_{\rm int}$) in the relation was estimated by adjusting its value to ensure $\chi^2_{\rm red} = 1$. A fuller description of the fitting procedure can be found in Williams et al. (2010) and Tiley et al. (2016a).

Since there is a significant bias in the slope of the forward fit (Willick 1994), we also fit the inverse of Equation 7 (similarly to Williams et al. 2010; Davis et al. 2011; Tiley et al. 2016a). In addition, we performed a number of further fits with the slope fixed to that of past studies (Tully & Pierce 2000,Tiley et al. 2016a and Torii et al., in prep.). The $K_{\rm s}$-band TFRs of the initial and final sub-samples are shown in Figure 1 along with fixed-slope fits. The fit parameters are listed in Table 3. While we list the results of both the forward and reverse fits in the table, we shall restrict our discussion to the more robust reverse fits.

As for $M_{K_{\rm s}}$, we also constructed stellar and baryonic mass TFRs for both the initial and final galaxy sub-samples, where $\log(M_\star/M_\odot)$ and $\log(M_{\rm b}/M_\odot)$ are, respectively, on the left hand side of Equation 7 instead (see Fig. 1 and Table 4).

The $M_{K_{\rm s}}$, $M_\star$ and $M_{\rm b}$ CO TFRs of the final sub-sample presented in Fig. 1 and Tables 3 and 4 constitute the main results of this paper, the first CO TFRs beyond the immediate local Universe.

5 DISCUSSION

A relation between luminous and dynamical (i.e. total) mass, the TFR informs us about both the structural and the dynamical properties of galaxies, particularly the total mass surface density and total mass-to-light ratio (and thus all properties affecting this ratio, including the stellar M/L, gas content and dark matter content). Comparing the TFRs measured for different galaxy samples thus reveals differences in those properties. These differences are, however, also tightly connected to the way the samples were selected. For example, comparing the TFRs of galaxies of different morphological types at a given redshift will inform on differences between those types (e.g. Russell 2004; Shen et al. 2009; Lagattuta et al. 2013), while comparing the TFRs of galaxies of a given type at different redshifts will inform on the evolution of those galaxies (e.g. Conselice et al. 2005; Flores et al. 2006; Puech et al. 2008). Similarly, luminosities for a given sample measured in different bands will inform on the stellar M/L. However, when comparing different TFRs, one must make sure that all the parameters used (e.g. luminosity, rotation velocity, inclination, and any corrections to those) are measured or calculated in an identical manner, as otherwise any difference between the zero-points and/or slopes of different TFRs could be due to different systematics between the methods used rather than any intrinsic physical differences between the samples. With those caveats in mind, we compare our results to others in the literature below.

Table 3. Best-fit parameters of the K_s-band CO TFRs.

Sub-sample	Fit type	Slope	Zero-point (mag)	$\sigma_{\rm int}$ (mag)	$\sigma_{\rm total}$ (mag)	Zero-point offset (Ours - Theirs)
Initial	Forward	-1.49 ± 0.61	-24.66 ± 0.14	0.76 ± 0.09	0.75 ± 0.03	–
	Reverse	-11.07 ± 4.58	-23.63 ± 0.60	2.03 ± 0.27	2.08 ± 0.16	–
		(-16.50 ± 9.77)	(-22.57 ± 1.46)	(2.78 ± 0.29)	(2.85 ± 0.41)	–
Final	Forward	-2.31 ± 0.78	-24.47 ± 0.19	0.68 ± 0.11	0.68 ± 0.03	–
	Reverse	-8.43 ± 2.86	-23.47 ± 0.54	1.31 ± 0.10	1.30 ± 0.09	–
		(-16.40 ± 4.76)	(-21.04 ± 1.16)	(0.94 ± 0.10)	(1.01 ± 0.19)	–
	Fixed (Ti16)	-7.1	-24.26 ± 0.22	1.08 ± 0.04	1.10 ± 0.04	-0.43 ± 0.24
			(-23.84 ± 0.16)	(0.64 ± 0.00)	(0.67 ± 0.03)	(-0.01 ± 0.18)
	Fixed (TP00)	-8.8	-23.42 ± 0.28	1.34 ± 0.10	1.35 ± 0.05	-0.25 ± 0.52
			(-22.87 ± 0.17)	(0.63 ± 0.10)	(0.68 ± 0.04)	(0.30 ± 0.47)
Bin A Final	Forward	-1.92 ± 0.55	-24.65 ± 0.14	0.35 ± 0.11	0.34 ± 0.03	–
	Reverse	-3.10 ± 0.85	-24.52 ± 0.18	0.44 ± 0.09	0.43 ± 0.04	–
		(-7.15 ± 2.12)	(-23.47 ± 0.50)	(0.21 ± 0.10)	(0.23 ± 0.10)	–
	Fixed (Ti16)	-7.1	-24.64 ± 0.40	1.22 ± 0.10	1.20 ± 0.08	-0.81 ± 0.41
			(-24.04 ± 0.11)	(0.15 ± 0.02)	(0.23 ± 0.03)	(-0.18 ± 0.14)
	Fixed (TP00)	-8.8	-23.89 ± 0.52	1.59 ± 0.02	1.56 ± 0.14	-0.72 ± 0.68
			(-23.10 ± 0.15)	(0.21 ± 0.00)	(0.30 ± 0.03)	(0.08 ± 0.46)
Bin B Final	Forward	-3.03 ± 1.57	-24.04 ± 0.37	0.78 ± 0.17	0.73 ± 0.19	–
	Reverse	-10.99 ± 5.69	-22.56 ± 1.15	1.49 ± 0.10	1.40 ± 0.37	–
		(-11.95 ± 2.80)	(-21.73 ± 0.72)	(0.59 ± 0.10)	(0.63 ± 0.25)	–
	Fixed (Ti16)	-7.1	-23.89 ± 0.31	1.03 ± 0.10	1.03 ± 0.06	-0.05 ± 0.32
			(-23.48 ± 0.18)	(0.51 ± 0.01)	(0.54 ± 0.05)	(0.35 ± 0.20)
	Fixed (TP00)	-8.8	-23.01 ± 0.36	1.21 ± 0.10	1.20 ± 0.08	0.16 ± 0.56
			(-22.50 ± 0.18)	(0.47 ± 0.10)	(0.53 ± 0.06)	(0.67 ± 0.48)
	Fixed (Bin A)	-3.1	-24.07 ± 0.23	0.79 ± 0.07	0.77 ± 0.06	0.45 ± 0.29

Notes: Ti16: Tiley et al. (2016a), TP00: Tully & Pierce (2000). Values in parentheses are for the reverse fits after excluding the outliers (see Section 5.2).

Table 4. Best-fit parameters of the $M_\star$ and $M_{\rm b}$ CO TFRs

	Sub-sample	Fit type	Slope	Zero-point $\log(M/M_\odot)$	$\sigma_{\rm int}$ $\log(M/M_\odot)$	$\sigma_{\rm total}$ $\log(M/M_\odot)$	Zero-point offset (Ours - Theirs)
$M_\star$ CO TFRs	Initial	Forward	0.60 ± 0.27	10.81 ± 0.06	0.33 ± 0.05	0.35 ± 0.01	
		Reverse	5.59 ± 2.64	10.27 ± 0.33	1.03 ± 0.14	1.08 ± 0.11	
			(5.60 ± 2.38)	(10.09 ± 0.38)	(0.90 ± 0.14)	(0.94 ± 0.11)	
	Final	Forward	0.55 ± 0.34	10.84 ± 0.08	0.29 ± 0.05	0.30 ± 0.02	
		Reverse	5.18 ± 3.00	10.08 ± 0.52	0.90 ± 0.15	0.89 ± 0.10	
			(6.06 ± 1.54)	(9.51 ± 0.38)	(0.31 ± 0.09)	(0.36 ± 0.06)	
		Fixed (Ti16)	3.3	10.65 ± 0.12	0.57 ± 0.12	0.58 ± 0.02	0.14 ± 0.13
				(10.44 ± 0.06)	(0.22 ± 0.09)	(0.27 ± 0.01)	(-0.07 ± 0.07)
	Bin A Final	Reverse	-22.13 ± 166.57	13.23 ± 18.25	5.40 ± 0.30	4.93 ± 4.34	
			(11.37 ± 16.86)	(8.25 ± 3.78)	(0.86 ± 0.27)	(0.74 ± 1.24)	
		Fixed (Ti16)	3.3	10.73 ± 0.26	0.79 ± 0.18	0.78 ± 0.08	0.22 ± 0.26
				(10.35 ± 0.15)	(0.28 ± 0.12)	(0.30 ± 0.04)	(-0.15 ± 0.16)
	Bin B Final	Reverse	4.35 ± 2.04	10.11 ± 0.42	0.57 ± 0.15	0.55 ± 0.13	
			(4.91 ± 1.19)	(9.75 ± 0.31)	(0.23 ± 0.11)	(0.26 ± 0.10)	
		Fixed (Ti16)	3.3	10.57 ± 0.13	0.42 ± 0.14	0.43 ± 0.03	0.06 ± 0.14
				(10.41 ± 0.08)	(0.19 ± 0.10)	(0.23 ± 0.02)	(-0.09 ± 0.10)
$M_{\rm b}$ CO TFRs	Initial	Forward	0.55 ± 0.23	10.92 ± 0.05	0.29 ± 0.04	0.30 ± 0.01	
		Reverse	4.96 ± 2.42	10.45 ± 0.30	0.92 ± 0.12	0.95 ± 0.06	
			(4.78 ± 1.98)	(10.32 ± 0.31)	(0.76 ± 0.10)	(0.80 ± 0.08)	
	Final	Forward	0.51 ± 0.31	10.93 ± 0.08	0.27 ± 0.05	0.28 ± 0.02	
		Reverse	4.86 ± 2.83	10.23 ± 0.50	0.85 ± 0.14	0.83 ± 0.12	
			(5.30 ± 1.11)	(9.78 ± 0.28)	(0.23 ± 0.05)	(0.28 ± 0.06)	

Notes: Ti16: Tiley et al. (2016a). Values in parentheses are for the reverse fits after excluding the outliers (see Section 5.2).

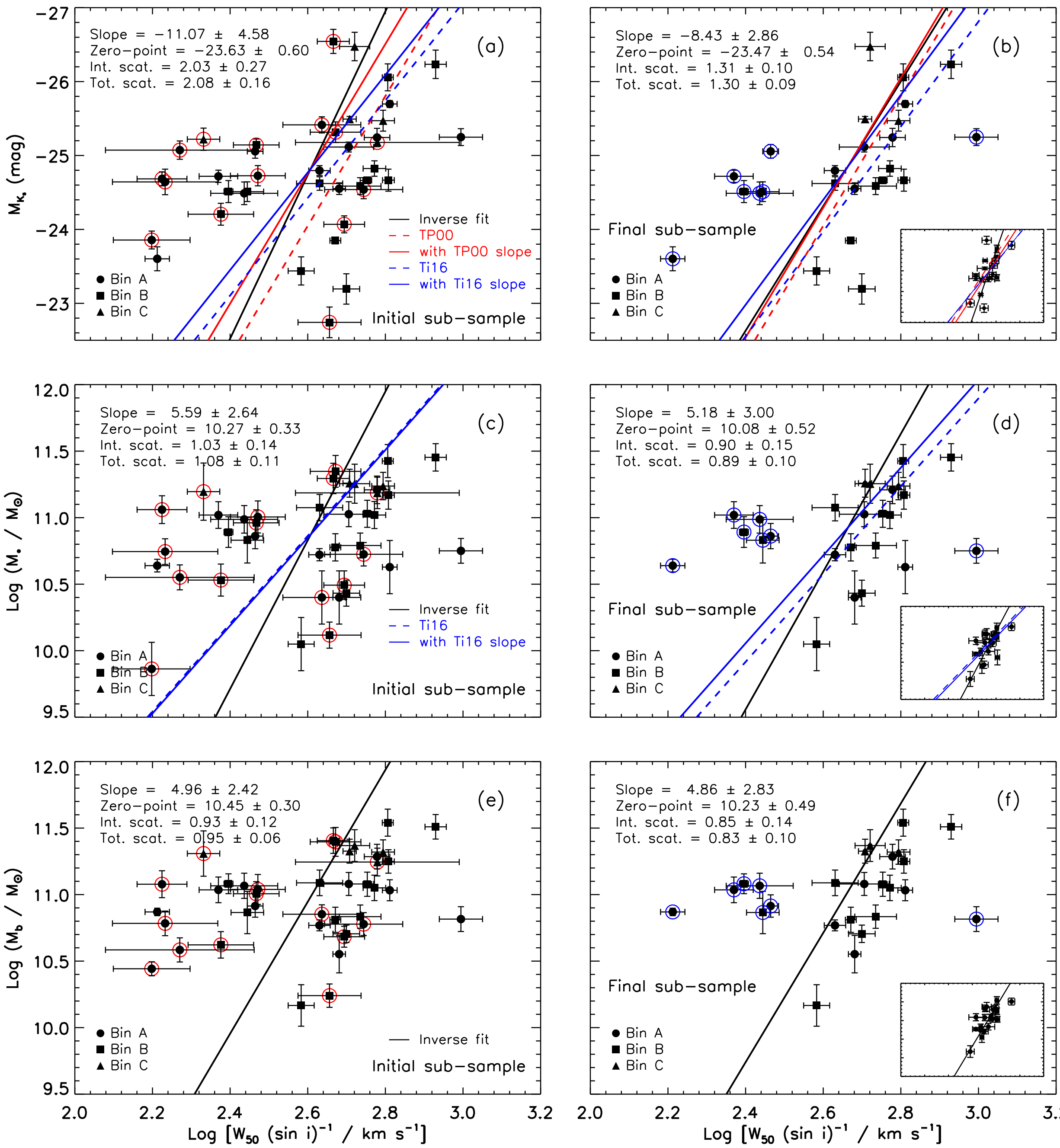

Figure 1. Top: K_s-band CO TFR of the initial (left) and final (right) galaxy sub-samples. The black solid lines show the reverse fits, while the red (respectively blue) lines show the reverse fit with slope fixed to that of Tully & Pierce (2000) (resp. Tiley et al. 2016a). The red dashed lines show the H I TFR of local spirals from Tully & Pierce (2000). The blue dashed lines show the CO TFR of local spirals (Tiley et al. 2016a). **Middle**: As for the top panels, but for the $M_\star$ CO TFR. **Bottom**: As for the top and the middle panels, but for the M_b CO TFR. In panels (a), (c) and (e), the data points with open red circles represent galaxies with a single Gaussian line profile, while open blue circles in panels (b), (d) and (f) represent the outliers (see Section 5.2). In all panels, the black filled circles, black filled squares and black filled triangles show the galaxies in bin A, bin B and bin C, respectively. All the fits shown were done with all the data points. The embedded figures in panels (b), (d) and (f) show the TFR for the final galaxy sub-sample after excluding the outliers.

5.1 Previous studies

The literature on the TFR is vast, but the number of studies using CO as the kinematic tracer is small. The most recent studies are those of Davis et al. (2011), Tiley et al. (2016a) and Torii et al. (in prep.). Davis et al. (2011) studied ETGs, however, so we will refrain from a comparison here as we would be unable to assign any difference to a redshift evolution rather than structural differences, or vice-versa. Tiley et al. (2016a) and Torii et al. (in prep.) also targeted disc galaxies and measured the velocity widths in a manner identical to us. They are thus best suited for comparison. The sam-

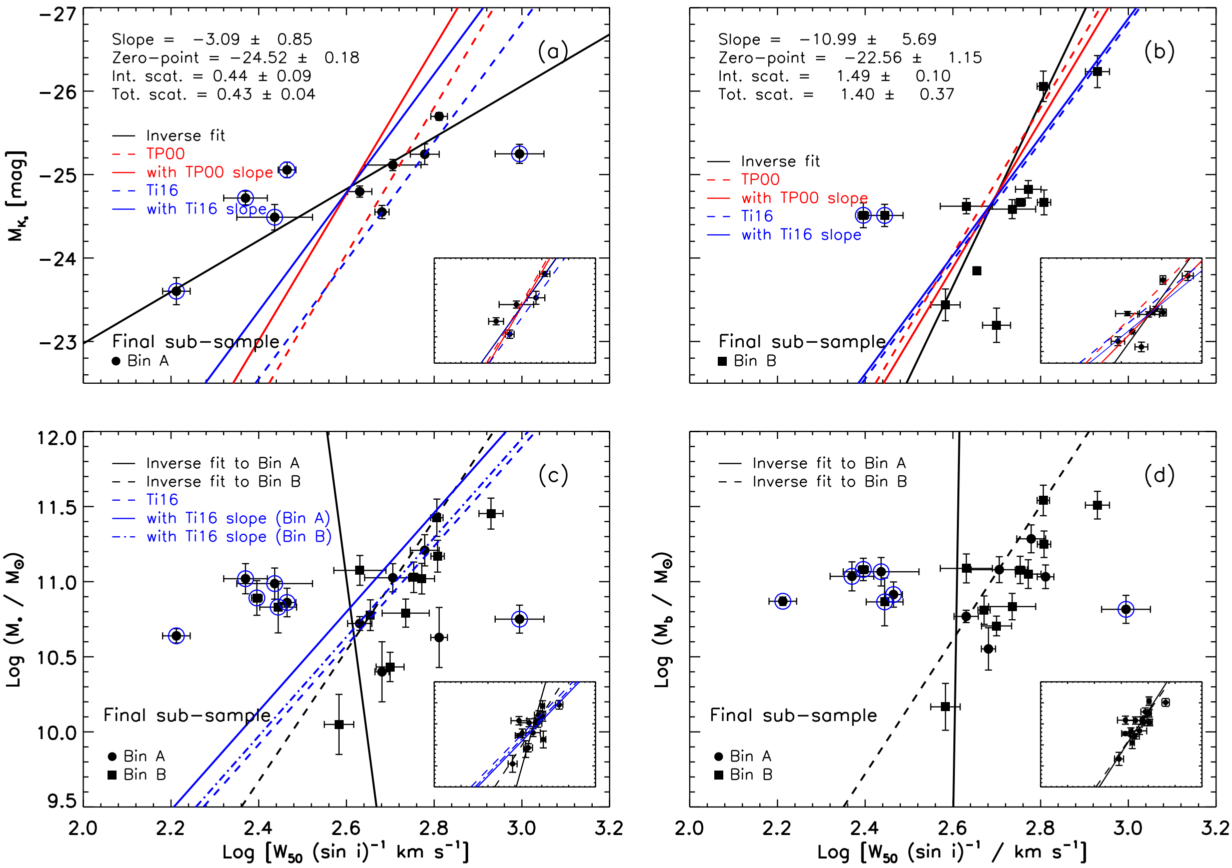

Figure 2. Top: K_s-band CO TFR of bin A (left) and bin B (right) galaxies only in the final sub-sample. The black solid lines show the reverse fits, while the red (respectively blue) lines show the reverse fit with slope fixed to that of Tully & Pierce (2000) (resp. Tiley et al. 2016a). The red dashed lines show the H I TFR of local spirals from Tully & Pierce (2000). The blue dashed lines show the CO TFR of local spirals (Tiley et al. 2016a). **Bottom**: In panel (c), the $M_\star$ CO TFRs of the final sub-sample galaxies in bin A and bin B are shown in the same plot. Similarly, in panel (d) the M_b CO TFRs of the final sub-sample galaxies in bin A and bin B are shown in the same plot. In both panels (c) and (d), the black solid lines and black dashed lines show the reverse fits for the final sub-sample galaxies in bin A and bin B, respectively. In panel (c), the blue solid line and the blue dot-dashed line shows the reverse fit with slope fixed to that of Tiley et al. (2016a) for the final sub-sample galaxies in bin A and bin B, respectively. The blue dashed line in panel (c) shows the CO TFR of Tiley et al. (2016a), as for the top panels. In all panels, the black filled circles and black filled squares show the final sub-sample galaxies in bin A and bin B, respectively. In all panels, the data points shown as open blue circles represent the outliers (see Section 5.2). The embedded figures in all panels show the TFR of the final sub-sample galaxies in bin A and bin B after excluding the outliers.

ple of Tiley et al. (2016a) is composed of ≈ 300 disc galaxies from the CO Legacy Database for the GALEX Arecibo SDSS survey (GASS, Catinella et al. 2010; COLD GASS, Saintonge et al. 2011) and they used the Wide-Field Infrared Survey Explorer (WISE) Band 1 ($W1$, ≈ 3.4µm) to construct their TFR. Although the $W1$ band is not identical to the 2MASS K_s band (≈ 2.4µm), both filters trace similar stellar populations and $K - W1 \approx 0.0 \pm 0.2$ mag for late-type galaxies (Lagattuta et al. 2013), so a direct comparison is appropriate. Torii et al. (in prep.) studied ≈ 50 late-type nearby galaxies and also used 2MASS K_s-band magnitudes, but their study is not finalised yet and so will not be considered further.

At a fixed stellar mass, galaxies are generally smaller at higher redshifts. The COLD GASS galaxies of Tiley et al. (2016a) are all located at $z \approx 0.03$ and have an average effective (half-light) radius (R_e) of $2.''6$ (based on SDSS r-band photometry), corresponding to a linear size of 1.6 kpc at an average distance of ≈ 130 Mpc (based on the cosmology calculator of Wright 2006). On the other hand, all galaxies in our sample, located $z = 0.05$–0.3, have $R_e > 1.6$ kpc. This suggests that our galaxies are both CO bright and larger on average than Tiley et al.'s (2016a) galaxies.

Despite their use of H I rather than CO, we also discuss the work of Tully & Pierce (2000) below, as it is generally considered the standard reference on the subject. Tully & Pierce measured the velocity width at 20% of the peak (rather than 50% as done here). While the difference is generally small, the velocity width at 20% of the peak is systematically larger.

5.2 Outliers

As seen from Figure 1, there are a few low-velocity galaxies and one high-velocity galaxy that appear to constitute clear outliers with respect to the general trend in the data. Those galaxies with velocities $2.5 \geqslant \log(W_{50} \sin^{-1} i \,/\, \mathrm{km\ s^{-1}}) \geqslant 3.0$ are listed in Tables 1 and 2 (i.e. galaxies labeled as G1, G3, G4, G5, G11, G24 and G25). We examine the properties of those 7 galaxies and then the

TFR results with/without them, to better understand whether they are intrinsically different.

Five out of seven galaxies are located at $z \leqslant 0.1$, while the remaining two galaxies are located at $z \approx 0.2$. The SFRs of the galaxies range from 5 to 56 $M_{\odot}$ yr^{-1}, except one galaxy (G24) with a very low SFR of 0.02 $M_{\odot}$ yr^{-1}. Very high inclinations can bias photometric measurements due to internal absorption, but the outlier galaxies have inclinations ranging from 43 to 65°, except one galaxy (G24) with a relatively high inclination of 84°. Furthermore, the stellar and baryonic masses of the outliers are similar to those of the other galaxies in the final sub-sample (see Table 2). Overall, the outliers thus seem unremarkable.

The embedded panels in Figures 1 and 2 represent the TFR fits to the data after excluding the 7 outliers. The results based on those fits are also listed in Tables 3 and 4 (values shown in parentheses) and are discussed in the following sub-sections.

5.3 Evolution with redshift

Some early works suggest an evolution (i.e. a different zero-point and/or slope) of the B-band TFR at intermediate redshifts, in the sense that higher redshift galaxies are brighter at a given rotational velocity (e.g. Vogt et al. 1996; Simard & Pritchet 1998; Ziegler et al. 2002; Milvang-Jensen et al. 2003; Böhm et al. 2004; Bamford et al. 2006), although it may be that only low-mass systems show such an offset (Ziegler et al. 2002; Böhm et al. 2004). Furthermore, Ziegler et al. (2002) studied the B-band TFR of 60 late-type galaxies at $z = 0.1$–1.0, and found that the slope is flatter for distant galaxies. More recent works however seem to indicate that there is no redshift evolution in the K-band relation (e.g. Conselice et al. 2005; Flores et al. 2006; Tiley et al. 2016a; but see Puech et al. 2008 who found that $z \approx 0.6$ galaxies are *fainter* than local galaxies by 0.66 ± 0.14 mag at K-band). There is thus clearly some disagreement in the literature as to whether the TFR evolves with redshift or not.

5.3.1 Evolution in slope and luminosity

As the galaxies in our samples cover a reasonable range in redshift ($z = 0.3$ corresponds to a ≈ 3.5 Gyr lookback time), it is possible to probe whether the TFR has evolved during that period by simply breaking down our galaxy samples by redshift. We therefore split our samples into three redshift bins and constructed the CO TFR for each bin separately (Fig. 2). Bin A includes galaxies at $z = 0.05$–0.1, bin B galaxies at $z = 0.1$–0.2, and bin C galaxies at $z = 0.2$–0.3 (the black filled circles, black filled squares and black filled triangles in Fig. 1, respectively). Bin A includes 17 galaxies (10 galaxies with a double-horned profile), bin B 18 galaxies (12 galaxies with a double-horned profile), but in bin C only 5 galaxies (3 galaxies with a double-horned profile), not enough for a reliable fit. The average galaxy SFRs are also different from each other, 14, 18 and 31 $M_{\odot}$ yr^{-1} for bin A, B and C, respectively, while COLD GASS galaxies have an average SFR of ≈ 4 $M_{\odot}$ yr^{-1}. Interestingly, the galaxies in bin A have masses similar to each other (both stellar and baryonic) despite a wide range of rotational velocities, causing the rather flat distributions in the $M_{K_{\rm s}}$, $M_{\star}$ and $M_{\rm b}$ CO TFRs (Fig. 2). The galaxies in bin B have a wider range of masses but a relatively narrow range of rotational velocities (Fig. 2).

The limitations described above lead to unreliable fits for individual bins (see Tables 3 and 4), and the slopes are essentially unconstrained (very large uncertainties). Nevertheless, it is possible to constrain zero-point offsets by using a unique slope across all bins. Fixing the slope of the final sub-sample reverse fit in bin B to that of bin A, we found a zero-point offset of 0.45 ± 0.29 mag (bin B - bin A), indicating that the galaxies in bin B are on average about 1.5 times fainter than those in bin A. However, this offset is not statistically significant, i.e. S/N < 3.

We also examined the galaxies in bin A and bin B only after excluding the outliers. Except for the smaller scatters (as expected by construction), we again found no significant change in the slopes and zero-points (see Table 3).

The other way to test for redshift evolution is to compare our results with those of other studies of local galaxies, although we must then be aware of differences between the samples and/or methods. Comparing to the TFR studies discussed above (Section 5.1), our results (see Table 3) indicate that the slope of the reverse $K_{\rm s}$-band CO TFR of the final sub-sample is consistent with that of nearby disc galaxies within the uncertainties (that are however quite large; e.g. Tully & Pierce 2000; Tiley et al. 2016a; see also Ziegler et al. 2002). This therefore suggests that there is no significant evolution of the slope of the TFR between local spirals and the galaxies in our final sub-sample at $z = 0.05$–0.3. When different redshift bins are considered, the slope of the reverse $K_{\rm s}$-band CO TFR of bin A is somewhat flatter than all the other samples, but this difference disappears when excluding the outliers from bin A and is thus doubtful (see Fig. 2 and Table 3).

Fixing the slope of the reverse fit to that of the spirals in Tiley et al. (2016a) and Tully & Pierce (2000), we found a zero-point offset (our fit minus theirs) of -0.43 ± 0.24 and -0.25 ± 0.52 mag, respectively (-0.01 ± 0.18 and 0.30 ± 0.47 mag, respectively, after excluding the outliers; see Table 3). Tiley et al. (2016a) being the study most similar to ours, this suggests that, at a given rotation velocity, our final sub-sample galaxies are on average brighter than local galaxies by ≈ 0.43 mag or a factor of about 1.5. As expected from the comparisons of bin A and bin B galaxies above, when fixing the slope to that of the spirals of Tiley et al. (2016a) and repeating the fit for bin A galaxies only, we find a larger zero-point offset of -0.81 ± 0.41 mag (-0.18 ± 0.14 mag after excluding the outliers), a factor of slightly more than two in luminosity, while the offset between the galaxies in bin B and Tiley et al. (2016a) is negligible, i.e. -0.05 ± 0.32 mag (0.35 ± 0.20 mag after excluding the outliers). All these offsets are listed in Table 3, but none is truly significant.

5.3.2 Evolution in mass

We now turn our attention to the $M_{\star}$ and $M_{\rm b}$ CO TFRs (see Fig. 1). The slope of the $M_{\star}$ CO TFR for our final galaxy sub-sample is similar to that of Tiley et al. (2016a) for local spiral galaxies. In addition, fixing the slope to that of Tiley et al. (2016a), we find a zero-point offset (our fit minus their) of 0.14 ± 0.13 dex (-0.07 ± 0.07 dex after excluding the outliers; see Table 4), indicating no significant evidence for evolution of the $M_{\star}$ TFR zero-point since $z \approx 0.3$. If we probe the offset between bin A and Tiley et al. (2016a) galaxies, we obtain an offset of 0.22 ± 0.26 dex (-0.15 ± 0.16 dex after excluding the outliers). For bin B galaxies, we obtain an offset of 0.06 ± 0.14 dex (-0.09 ± 0.10 dex after excluding the outliers). All results based on the final sub-sample thus arrive the same conclusion: no offset in stellar mass.

The results for the $M_{\rm b}$ CO TFRs agree with those of the $M_{\star}$ CO TFRs, i.e. same slopes and zero-points within the uncertainties, but with slightly smaller scatters. The results after excluding the outliers also indicate the same slopes and zero-points within the uncertainties (see Table 4). Since, there is no baryonic mass CO

TFR in the literature, we shall not discuss this relation further. Otherwise, any comparison between $M_{\rm b}$ TFR studies exploiting other kinematic tracers would introduce too many potential systematics.

Overall, when all galaxies in the final sub-sample are considered, and given the large uncertainties in the offsets found, our results for the $K_{\rm s}$-band, $M_\star$ and $M_{\rm b}$ CO TFRs suggest no significant redshift evolution in either luminosity or mass (even after excluding the outliers).

As they were selected to be on the upper envelope of the star-formation main sequence at their redshifts (Bauermeister et al. 2013), and as the SFR of the main sequence increases with redshift (e.g. Noeske et al. 2007), one would naively have expected the higher redshift galaxies to have slightly lower stellar (and thus dynamical) M/L. This would naturally explain any brightening in luminosity with z, but would not predict a commensurate increase in mass (as the stellar M/L of our sample galaxies would then be lower than those of local galaxies). This effect is not observed here, presumably because of a combination of the relatively small coverage in redshift and the relatively large uncertainties in the data (and thus TFRs).

5.4 Intrinsic scatter

As can be seen from Table 3, the intrinsic scatter of the reverse $K_{\rm s}$-band CO TFR of the final sub-sample ($\sigma_{\rm int} = 1.3$) is higher than that of Tiley et al. (2016a) ($\sigma_{\rm int} = 0.7$) and Davis et al. (2011) ($\sigma_{\rm int} = 0.6$). The reasons for this relatively higher scatter are unclear, since the final sub-sample only contains galaxies that should yield robust measurements, but we can speculate. In fact, the scatter decreases to a comparable or even lower value when the outliers are excluded, particularly when different redshift bins are considered (see Table 3).

The TFR is known to have a much greater scatter at higher redshifts (e.g. Tiley et al. 2016b), this for a variety of reasons such as greater variations of the stellar mass fraction (and thus total M/L ratio) and stellar M/L ratio, and most importantly increased morphological and dynamical anomalies (e.g. Kannappan et al. 2002; Flores et al. 2006; Kassin et al. 2007). It could thus be that some of these effects are already significant at $z \lesssim 0.3$.

Our inclinations derived from the stellar axial ratios could also introduce more scatter than superior measurements (e.g Davis et al. 2011), although as long as the uncertainties are properly quantified this should only affect the total scatter ($\sigma_{\rm total}$) and not the intrinsic scatter ($\sigma_{\rm int}$). In addition, due to the difficulty of identifying interacting and/or disturbed galaxies at the modest resolution of SDSS, it is possible that despite our best efforts to exclude them some interacting galaxies do remain in the initial and final samples. Overall, however, the main reason behind the large intrinsic scatter measured remains unclear.

5.5 Inclinations

In view of the comments in Section 5.4, it is worth noting that the accuracy of the TFR fits strongly depends on the accuracy of the inclination measurements, as the circular velocity measurements (here the velocity widths) must be corrected for the inclination of the galaxies. We used here stellar axial ratios to estimate the inclinations, as is common in the literature (e.g. Tully & Pierce 2000; Davis et al. 2011; Tiley et al. 2016a). Although these inclinations can lead to a large scatter in the TFR, they do not generally affect its slope and/or zero-point (e.g. Davis et al. 2011). For our sample, the slope and zero-point obtained for the initial sub-sample are consistent with those of the final sub-sample within the uncertainties (see Tables 3 and 4), indicating that our results are indeed robust and only minimally affected by inclination uncertainties.

We assumed a value of 0.2 for q_0 (i.e. we assumed late-type systems; Tully & Fisher 1977; Pierce & Tully 1988). However, it is clear that any variation in q_0 will affect the inclinations inferred, and thus the TFR results. We investigated this effect and found that the effect is very small. For example, assuming $q_0 = 0$ would yield the same zero-point and slope for both the initial and final sub-samples within the errors. In particular, the change in the zero-points are tiny. Similarly, if we assume $q_0 = 0.34$ (as for ETGs; Davis et al. 2011), the results for the slopes and zero-points are again unchanged within the errors. This indicates that q_0 uncertainties have an insignificant effect on the inclination-corrected velocities and thus our TFR results.

6 CONCLUSIONS

We studied the $K_{\rm s}$-band, stellar mass and baryonic mass CO TFRs of 25 carefully selected galaxies at $z \approx 0.05$–0.3, and compared our results to those obtained for similar local disc galaxy samples. This represents the first attempt to construct TFRs for disc galaxies beyond the local universe using CO as a kinematic tracer. The principal results are summarised below.

(i) The best-fit reverse $K_{\rm s}$-band, stellar mass and baryonic mass TFRs are $M_{K_{\rm s}} = (-8.4 \pm 2.9)\left[\log\left(\frac{W_{50}/\mathrm{km\ s^{-1}}}{\sin i}\right) - 2.5\right] + (-23.5 \pm 0.5)$, $\log(M_\star/M_\odot) = (5.2 \pm 3.0)\left[\log\left(\frac{W_{50}/\mathrm{km\ s^{-1}}}{\sin i}\right) - 2.5\right] + (10.1 \pm 0.5)$ and $\log(M_{\rm b}/M_\odot) = (4.9 \pm 2.8)\left[\log\left(\frac{W_{50}/\mathrm{km\ s^{-1}}}{\sin i}\right) - 2.5\right] + (10.2 \pm 0.5)$, respectively, where $M_{K_{\rm s}}$ is the total absolute $K_{\rm s}$-band magnitude of the objects, $M_\star$ and $M_{\rm b}$ their total stellar and baryonic mass, respectively, and W_{50} the width of their integrated CO line profile at 50% of the maximum.

(ii) When different redshift bins are considered within our sample, we find no significant change in the slope or zero-point of the TFRs, in either luminosity or mass.

(iii) When comparing to other TFR studies of local ($z = 0$) disc galaxies, we again find no significant offset in either luminosity or mass.

(iv) Similarly to galaxies at much higher redshifts, our sample galaxies show higher intrinsic scatters around the best-fit TFRs than local galaxies. The main drivers of this are also likely analogous, i.e. higher gas fractions coupled with more intense star formation, and morphological as well as dynamical disturbances.

(v) Although the scatter in the $M_{K_{\rm s}}$ TFR is high compared to that of local studies, the scatter decreases to comparable and even lower values when obvious outliers are excluded, particularly for the case of different redshift bins, thus suggesting that the increased scatter is due to a few pathological galaxies rather than the general galaxy population.

More generally, our study supports the view that CO is an excellent kinematical tracer for TFR studies. As CO is relatively easy to detect even in distant galaxies, our study provides a useful benchmark for future high-redshift CO TFR studies, themselves a powerful tool to probe the cosmological evolution of the M/L of galaxies.

ACKNOWLEDGEMENTS

The authors would like to thank the anonymous referee for his/her insightful comments and suggestions. ST thanks to Amber Bauermeister for kindly providing the CO data for the EGNoG sample. ST was supported by the Republic of Turkey, Ministry of National Education, The Philip Wetton Graduate Scholarship at Christ Church, and also acknowledges support from Van 100. Yil University, project code: FBA-2017-5874. MB acknowledges support from STFC rolling grant Astrophysics at Oxford PP/E001114/1. AT acknowledges support from an STFC Studentship. This research made use of the NASA/IPAC Extragalactic Database (NED), which is operated by the Jet Propulsion Laboratory, California Institute of Technology, under contract with the National Aeronautics and Space Administration. This work is based in part on data obtained as part of the UKIRT Infrared Deep Sky Survey. This publication also makes use of data products from the Two Micron All Sky Survey, which is a joint project of the University of Massachusetts and the Infrared Processing and Analysis Center/California Institute of Technology, funded by the National Aeronautics and Space Administration and the National Science Foundation. This research also made use of SDSS-III data release. SDSS-III is managed by the Astrophysical Research Consortium for the Participating Institutions of the SDSS-III Collaboration including the University of Arizona, the Brazilian Participation Group, Brookhaven National Laboratory, Carnegie Mellon University, University of Florida, the French Participation Group, the German Participation Group, Harvard University, the Instituto de Astrofisica de Canarias, the Michigan State/Notre Dame/JINA Participation Group, Johns Hopkins University, Lawrence Berkeley National Laboratory, Max Planck Institute for Astrophysics, Max Planck Institute for Extraterrestrial Physics, New Mexico State University, New York University, Ohio State University, Pennsylvania State University, University of Portsmouth, Princeton University, the Spanish Participation Group, University of Tokyo, University of Utah, Vanderbilt University, University of Virginia, University of Washington, and Yale University.

REFERENCES

Abazajian K. N. et al., 2009, ApJSS, 182, 543
Alam S. et al., 2015, ApJS, 219, 12
Alonso-Herrero A., 2013, ArXiv:1302.2033
Armus L., Heckman T., Miley G., 1987, AJ, 94, 831
Baldwin J. A., Phillips M. M., Terlevich R., 1981, PASP, 93, 5
Balkowski C., Bottinelli L., Chamaraux P., Gouguenheim L., Heidmann J., 1974, A&A, 34, 43
Bamford S. P., Aragón-Salamanca A., Milvang-Jensen B., 2006, MNRAS, 366, 308
Bauermeister A. et al., 2013, ApJ, 768, 132
Bedregal A. G., Aragón-Salamanca A., Merrifield M. R., 2006, MNRAS, 373, 1125
Blanton M. R., Roweis S., 2007, AJ, 133, 734
Böhm A. et al., 2004, A&A, 420, 97
Brinchmann J., Charlot S., White S. D. M., Tremonti C., Kauffmann G., Heckman T., Brinkmann J., 2004, MNRAS, 351, 1151
Bruzual G., Charlot S., 2003, MNRAS, 344, 1000
Bushouse H. A. et al., 2002, ApJS, 138, 1
Carpineti A., Kaviraj S., Hyde A. K., Clements D. L., Schawinski K., Darg D., Lintott C. J., 2015, A&A, 577, A119
Casali M. et al., 2007, A&A, 467, 777
Catinella B. et al., 2010, MNRAS, 403, 683
Conselice C. J., Bundy K., Ellis R. S., Brichmann J., Vogt N. P., Phillips A. C., 2005, ApJ, 628, 160
Cortese L., Catinella B., Janowiecki S., 2017, ApJ, 848, L7
Davis T. A. et al., 2013, MNRAS, 429, 534
Davis T. A. et al., 2011, MNRAS, 414, 968
De Rijcke S., Zeilinger W. W., Hau G. K. T., Prugniel P., Dejonghe H., 2007, ApJ, 659, 1172
den Heijer M. et al., 2015, A&A, 581, A98
Dickey J. M., Kazes I., 1992, ApJ, 393, 530
Dressler A., Sandage A., 1983, ApJ, 265, 664
Flores H., Hammer F., Puech M., Amram P., Balkowski C., 2006, A&A, 455, 107
Genzel R. et al., 2015, ApJ, 800, 20
Gerhard O., Kronawitter A., Saglia R. P., Bender R., 2001, AJ, 121, 1936
Hinz J. L., Rieke G. H., Caldwell N., 2003, AJ, 126, 2622
Hinz J. L., Rix H.-W., Bernstein G. M., 2001, AJ, 121, 683
Ho L. C., 2007, ApJ, 669, 821
Hogg D. W., Baldry I. K., Blanton M. R., Eisenstein D. J., 2002, arXiv:astro-ph/0210394
Holmberg E., 1958, Meddelanden fran Lunds Astronomiska Observatorium Serie II, 136, 1
Jarrett T. H., Chester T., Cutri R., Schneider S., Skrutskie M., Huchra J. P., 2000, AJ, 119, 2498
Kannappan S. J., Fabricant D. G., Franx M., 2002, AJ, 123, 2358
Kassin S. A. et al., 2007, ApJ, 660, L35
Kauffmann G. et al., 2003, MNRAS, 346, 1055
Kennicutt, Jr. R. C., 1998, ARA&A, 36, 189
Lagattuta D. J., Mould J. R., Staveley-Smith L., Hong T., Springob C. M., Masters K. L., Koribalski B. S., Jones D. H., 2013, ApJ, 771, 88
Lavezzi T. E., Dickey J. M., 1997, AJ, 114, 2437
Lavezzi T. E., Dickey J. M., 1998, AJ, 116, 2672
Lawrence A. et al., 2007, MNRAS, 379, 1599
Magorrian J., Ballantyne D., 2001, MNRAS, 322, 702
Maraston C., 2005, MNRAS, 362, 799
Markwardt C. B., 2009, in Astronomical Society of the Pacific Conference Series, Vol. 411, Astronomical Data Analysis Software and Systems XVIII, Bohlender D. A., Durand D., Dowler P., eds., p. 251
Mathieu A., Merrifield M. R., Kuijken K., 2002, MNRAS, 330, 251
Matsui K., Sorai K., Watanabe Y., Kuno N., 2012, PASJ, 64, 55
Melnick J., Mirabel I. F., 1990, A&A, 231, L19
Milvang-Jensen B., Aragón-Salamanca A., Hau G. K. T., Jørgensen I., Hjorth J., 2003, MNRAS, 339, L1
Mirabel I. F., Booth R. S., Johansson L. E. B., Garay G., Sanders D. B., 1990, A&A, 236, 327
Mobasher B. et al., 2015, ApJ, 808, 101
Mould J. R., Akeson R. L., Bothun G. D., Han M., Huchra J. P., Roth J., Schommer R. A., 1993, ApJ, 409, 14
Neistein E., Maoz D., Rix H.-W., Tonry J. L., 1999a, AJ, 117, 2666
Neistein E., Maoz D., Rix H.-W., Tonry J. L., 1999b, AJ, 117, 2666
Noeske K. G. et al., 2007, ApJ, 660, L43
Noordermeer E., Verheijen M. A. W., 2007, MNRAS, 381, 1463
Pierce M. J., Tully R. B., 1988, ApJ, 330, 579
Pizagno J. et al., 2007, AJ, 134, 945
Planck Collaboration et al., 2016, A&A, 594, A13
Puech M. et al., 2008, A&A, 484, 173

Riechers D. A. et al., 2009, ApJ, 703, 1338
Roediger J. C., Courteau S., 2015, MNRAS, 452, 3209
Russell D. G., 2004, ApJ, 607, 241
Saintonge A. et al., 2011, MNRAS, 415, 32
Sanders D. B., Scoville N. Z., Soifer B. T., 1991, ApJ, 370, 158
Schlegel D. J., Finkbeiner D. P., Davis M., 1998, ApJ, 500, 525
Schoniger F., Sofue Y., 1994a, A&A, 283, 21
Schoniger F., Sofue Y., 1994b, A&A, 283, 21
Scoville N. et al., 2007, ApJS, 172, 1
Shen S., Wang C., Chang R., Shao Z., Hou J., Shu C., 2009, ApJ, 705, 1496
Simard L., Pritchet C. J., 1998, ApJ, 505, 96
Skrutskie M. F. et al., 2006, AJ, 131, 1163
Steinmetz M., Navarro J. F., 1999, ApJ, 513, 555
Strauss M. A. et al., 2002, ApJ, 124, 1810
Surace J. A., Sanders D. B., Evans A. S., 2000, ApJ, 529, 170
Tacconi L. J. et al., 2010, Nat, 463, 781
Tiley A. L., Bureau M., Saintonge A., Topal S., Davis T. A., Torii K., 2016a, MNRAS, 461, 3494
Tiley A. L. et al., 2016b, MNRAS, 460, 103
Tully R. B., Fisher J. R., 1977, A&A, 54, 661
Tully R. B., Pierce M. J., 2000, ApJ, 533, 744
Tutui Y., Sofue Y., 1997, A&A, 326, 915
Tutui Y., Sofue Y., Honma M., Ichikawa T., Wakamatsu K.-i., 2000, PASJ, 52, 803
Tutui Y., Sofue Y., Honma M., Ichikawa T., Wakamatsu K.-I., 2001, PASJ, 53, 701
Veilleux S., Kim D.-C., Sanders D. B., 2002, ApJS, 143, 315
Veilleux S., Sanders D. B., Kim D.-C., 1999, ApJ, 522, 139
Verheijen M. A. W., 2001, ApJ, 563, 694
Vogt N. P., Forbes D. A., Phillips A. C., Gronwall C., Faber S. M., Illingworth G. D., Koo D. C., 1996, ApJ, 465, L15
Wang J. L., Xia X. Y., Mao S., Cao C., Wu H., Deng Z. G., 2006, ApJ, 649, 722
Wang R. et al., 2011, AJ, 142, 101
Williams M. J., Bureau M., Cappellari M., 2010, MNRAS, 409, 1330
Willick J. A., 1994, ApJS, 92, 1
Willick J. A., Strauss M. A., 1998, ApJ, 507, 64
Wright E. L., 2006, PASP, 118, 1711
York D. G. et al., 2000, The Astronomical Journal, 120, 1579
Ziegler B. L. et al., 2002, ApJ, 564, L69

APPENDIX A: INTEGRATED CO PROFILES AND BEST FITS

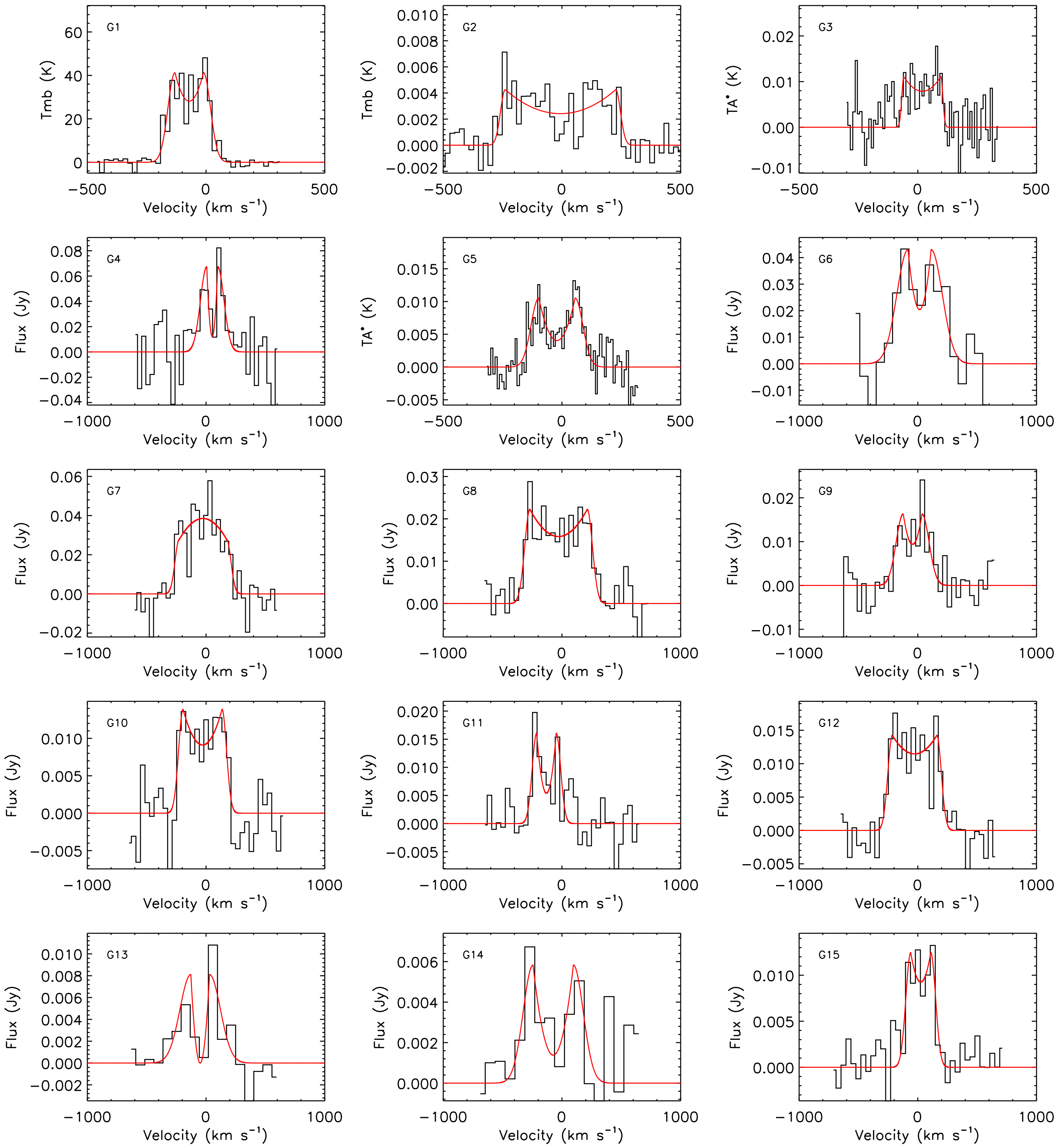

Figure A1. Integrated CO profiles of our initial sub-sample galaxies, taken from Bauermeister et al. (2013) and additional literature sources (see Section 2.2). For each plot, the red line shows the best parametric fit to the spectrum (see Section 4.1). The name of the galaxy as listed in Tables 1 and 2 is indicated in the top-left corner of each plot. The flux units are as in the original publications, but this has no bearing on the derived line widths.

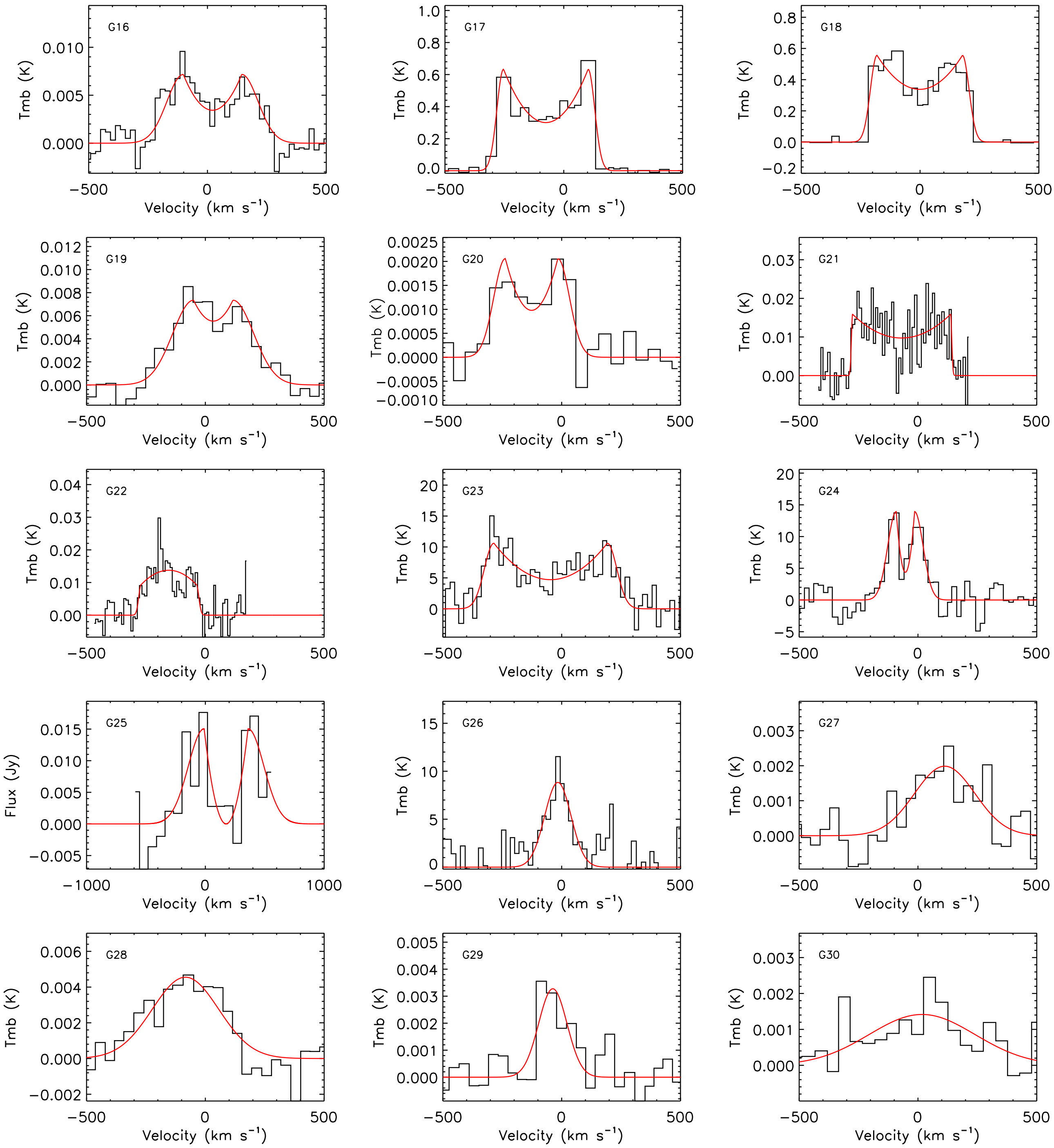

Figure A1. Continued.

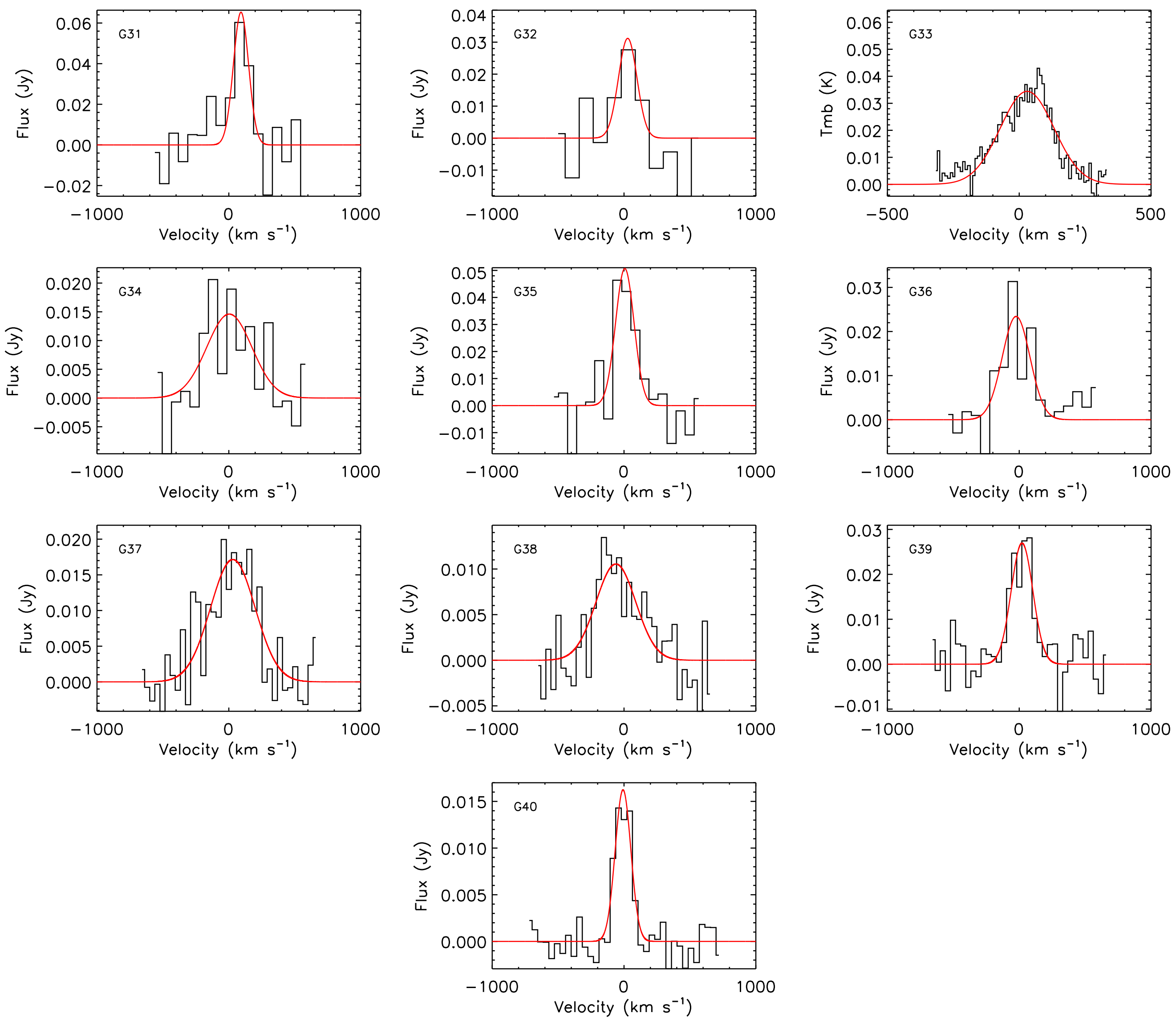

Figure A1. Continued.